A new capsule-intestine model for the capsule robot self-propelling in the lower gastrointestinal tract

Yao Yan[a], Ruifeng Guo[a], Jiyuan Tian[b], Yang Liu[b,*]

[a]*School of Aeronautics and Astronautics, University of Electronic Sci. and Technology of China, Chengdu, 611731, China*
[b]*Exeter Small-Scale Robotics Laboratory, Engineering Department, University of Exeter, Exeter, EX4 4QF, UK*

Abstract

Circular and haustral folds in the lower gastrointestinal tract (small and large intestines) are the major obstructions impeding the locomotion of the capsule robots for endoscopic diagnosis. Understanding the interactions between the capsule and these folds is critical for design and control of these robots to reach the areas of clinical interest. This paper proposes a new mathematical model of capsule-intestine interaction based on our previous work (Arch. Appl. Mech., 92:3861–3875) by introducing capsule's rotation during fold crossing. The resisting force of the fold predicted by the new model is more consistent with our finite element and experimental results compared to our previous model. It is found that the obstructive effect of the fold is stronger for a higher and thinner fold with a thinner and stiffer intestine. For the capsule robot, which is actuated by a periodically driven inner mass, a stronger excitation force is required to overcome the fold with a larger resisting force. Moreover, our bifurcation analysis reveals that a small excitation force always incurs a simple period-1 motion for the robot, while a large excitation force may result in various complex dynamics before the fold crossing. The findings of this work may help capsule robotics engineers to evaluate their designs in terms of propulsion and understand the locomotion of their robots in the lower gastrointestinal tract.

Keywords: Intestinal biomechanics; Capsule robot; Capsule endoscopy; Piecewise-smooth dynamical system; Bifurcation analysis.

1. Introduction

Lower gastrointestinal (GI) diseases, such as obscure GI bleeding, irritable bowel syndrome, diverticular disease, celiac disease, Crohn's disease, ulcerative colitis, polyposis syndromes and cancer plague many patients each year [1, 2]. According to Liu and Kaffes' work [3] on the diagnosis and evaluation of elusive GI bleeding, a substantial percentage of patients (21%) were not accurately diagnosed or were underestimated during clinical assessments. The incidence of GI bleeding is highest in the elderly population, particularly in the small intestine. Arteriovenous malformation or vascular dilatation accounts for 20% to 55% of intestinal bleeding cases, whereas small intestinal tumours are responsible for 10% to 20% of occurrences, making it the primary cause of morbidity in individuals under the age of 50. Individuals who suffer from celiac disease have a higher likelihood of developing microscopic colitis and inflammatory bowel disease (Crohn's disease and ulcerative colitis) [4]. In general, GI diseases, including tumours of the bowel, are typically associated with a specific syndrome that necessitates the management of internal intestinal manifestations [5]. Over the past two decades, capsule endoscopy technique has emerged as an effective method for detecting and diagnosing GI diseases [6]. Its advantages of being wireless, painless, safe, and fast make it a promising alternative to traditional endoscopes. In particular, the advent of active capsule robotics has improved the accuracy and functionality of endoscopies, such as biopsy, drug delivery, and cancer detection. However, a prerequisite for achieving these functions is the ability to precisely control its movement within the GI tract, which remains a challenging task for capsule robotics engineers [7].

*Corresponding author. Tel: +44(0)1392-724654, e-mail: y.liu2@exeter.ac.uk.

In order to control the motility of capsules within the GI tract, several propulsion mechanisms have been devised, including the paddle-type capsule [8], legged capsule [9], inchworm-like capsule [10], propeller-based capsule [11], vibration capsule [12, 13], and spiral-based capsule [14]. However, the majority of these methods for locomotion necessitate driving components positioned external to the capsule, including accessories like arms, fins, or propellers, all of which possess the potential to induce trauma to the intestinal environment. Consequently, the actively propelled capsule, featuring a whole smooth surface, emerges as a more patient-friendly and clinically acceptable resolution. Chernousko [15] has postulated that the rectilinear motion of a system can be achieved by governing the interaction between two rigid bodies in the presence of environmental resistance. This propulsion approach enables the inclusion of all driving components within an enclosed space. Widespread applications of this driving principle have been seen in vibro-impact drilling [16], capsule endoscopy [17], and pipeline inspection [18].

In the field of medical robotics, Liu et al. [12, 19] carried out a fundamental study on a vibro-impact capsule system, which is self-propelled without any external moving accessories. It achieves excitation through the internal magnet's periodic vibration and collision with the capsule's outer shell. When the interaction between the internal magnet and capsule shell exceeds the resistance provided by the intestinal tract, the entire capsule will undergo linear motion. The internal magnet is powered by an external coil positioned above the patient's abdomen, allowing manual movement by the clinician [20]. This handle coil can generate a periodic magnetic field under periodic electrical signals, such as square wave signals. Therefore, the clinician can control the capsule to move forward or backward by changing the driving parameters (e.g., amplitude, frequency, and duty cycle) of the electrical signal within the handle coil [21]. In addition, the direction of capsule propulsion can be controlled by adjusting the angle between the coil and the capsule [22]. At present, commercially accessible capsules [23], such as PillCam [24], typically have dimensions of 11 mm in diameter and 26 mm in length, becoming the standard for designing self-propelled capsule robots for intestinal diagnosis. Our team previously explored the vibro-impact capsule [25], following the same dimensions and features as these commercially available capsules. Prior research efforts have focused on enhancing the dynamic characteristics of the capsule, such as capsule's progression speed and energy efficiency under various control parameters [26–30].

However, the digestive system has complex anatomical features such as various obstacles in intestinal structures, which have been rarely considered in previous research. The digestive path from the mouth to the anus is known as the GI tract (also known as the digestive tract or alimentary canal) [31]. The human GI tract is comprised of the oesophagus, stomach, and intestines, and is commonly divided into the upper and lower GI tracts by clinicians to distinguish GI disease either from the upper or the lower tract [32]. The exact demarcation between the upper and lower tracts is the ligament of Treitz, also referred to as the suspensory ligament of the duodenum [33]. Thus, the lower GI tract includes most of the intestine. Within the realm of human anatomy, the intestine (also known as the bowel or gut) is composed of two distinct segments, namely the small intestine and the large intestine. It extends from the duodenum to the anus, which is a similar arrangement found in other mammals. The small intestine [31], about 6 metres in length and 3.5 centimetres in diameter, is further subdivided into the duodenum, jejunum, and ileum, coiling around the abdomen and extending the stomach to the colon, while the large intestine is subdivided into the cecum, ascending, transverse, descending and sigmoid colon, rectum, and anal canal [34].

In the small intestinal anatomy, the duodenum is about 25 centimetres in length as the first portion of the small intestine with no mesentery. The jejunum, connecting the duodenum and the ileum, is about 2.5 metres in length [35]. Compared to the other organs, the small intestine has a more complicated anatomy. The circular fold of the small intestine is a large valvular flap projected on the lumen of the intestine, which is about 2 millimetres in thickness [36]. It normally extends for about one half or two thirds of circumference of the small intestine showing in a crescent shape, but some may form a complete circle or in a spiral direction [35, 37]. Unlike the gastric fold in the stomach, the circular fold is permanent and does not disappear when the intestine is distended. The folds mainly distribute in the horizontal and ascending parts of the duodenum and the upper part of the jejunum per 25 millimetres in average [38, 39], and diminish considerably in size and quantity once reaching the middle of the ileum. Therefore, it is the main resistant mechanism for the endoscopic devices progressing in the small intestine. In addition, the large intestine also has its own folds, called haustral folds. These folds give the intestines

a segmented appearance. Each segment is a pouch formed through sacculation [40]. The separation between haustral folds exceeds that of circular folds in the small intestine, and unlike circular folds, haustral folds do not encircle the entire circumference of the intestine. They exhibit an increase in height along the proximal direction of the colon, with folds in the ascending and transverse colon notably taller than those observed in the descending colon [41]. In addition, intestinal tissue, including circular folds and haustral folds has different stiffness in different people and those with cancer [42]. The nature of these folds, their distribution in specific segments, and their role as a resistance mechanism highlight the need for a comprehensive exploration of capsule movement in this terrain. This sets the foundation for the subsequent investigation of dynamics of the capsule as it progresses through the intestine, an essential aspect of our exploration into the complex lower GI tract.

In the previous studies [43–46], the motion of the capsule robot on the intestine with folds did not consider capsule's rotation as a degree of freedom, resulting in a lack of the pitching phase compared to the actual situation. This led to the previous models incompletely characterising the capsule's motion, although with a general consistency. The primary aim of the present study is to propose a new model for the self-propelled capsule robot with the consideration of capsule's rotation, building upon our previous capsule-intestine contact model [43]. Based on the anatomical description of circular and haustral folds in the lower GI tract mentioned above, the present study will study the impacts of various intestinal features, including fold height and width, intestinal thickness, and intestinal Young's modulus, on the capsule's dynamics. By thoroughly investigating these factors, the goal is to understand their influences on the robot's propulsion process, especially when dealing with different types of intestines. Finally, through numerical simulations and bifurcation analyses, the dynamics of capsule interaction with folds have been explored. In the present work, some limitations observed in previous studies, particularly the lack of consideration of capsule's rotation and pitch angles, have been addressed, aiming to align the model more accurately with real-world scenarios. The results of this study may provide crucial insights for a better understanding of capsule's locomotion in the lower GI tract, offering a valuable guidance for the enhancement and optimisation of future capsule robot designs.

The remaining sections of this paper are organised as follows. Section 2 introduces the new mathematical model for the interaction between the capsule and the intestine, considering both movable and rotatable capsule interacting with a circular/hastral fold on a tissue substrate. The total resistance experienced by the capsule during this process is modelled at the head, tail, and cylindrical body of the capsule. Moreover, a dedicated model for the vibro-impact capsule is formulated. In Section 3, a comparison is made between the previous mathematical model, the newly proposed model, finite element analysis, and experimental results. The newly proposed model demonstrates a superior capability to characterise the capsule's motion during fold crossing. Furthermore, an exploration of the impact of fold parameters on capsule's resistance and bifurcation analyses studying the dynamics of capsule-fold interaction are conducted. Finally, conclusions are drawn in Section 4.

2. Method

2.1. Description of capsule-intestine interaction

Figure 1 illustrates a vibro-impact capsule robot moving horizontally in the x-direction (rightwards) on the lower GI tract with a thickness of H [mm] in the presence of a circular (or haustral) fold. As can be seen from the figure, the capsule has a cylindrical body with a length of L [mm] and a radius of R [mm], which connects its hemispheric head and tail. Since the capsule is very rigid compared with the soft tissue, it is assumed that the deformation of the incompressible and isotropic tissue conforms to the capsule profile. $\delta_{\max}$ [mm] is the depth at which the vertical base of centre of the capsule tail is embedded in the intestinal tissue in the y-direction. In front of the capsule at x_b [mm], the intestine has a circular fold with a height of h [mm] and a half-width of w [mm]. The shape function of the circular fold in Fig. 1(a) can be expressed as [47]

$$f(x,z)=\begin{cases} h\cos\left(\frac{x-x_{\mathrm{b}}}{2w}\pi\right), & |x-x_{\mathrm{b}}|\le w,\\ 0, & |x-x_{\mathrm{b}}|>w. \end{cases} \tag{1}$$

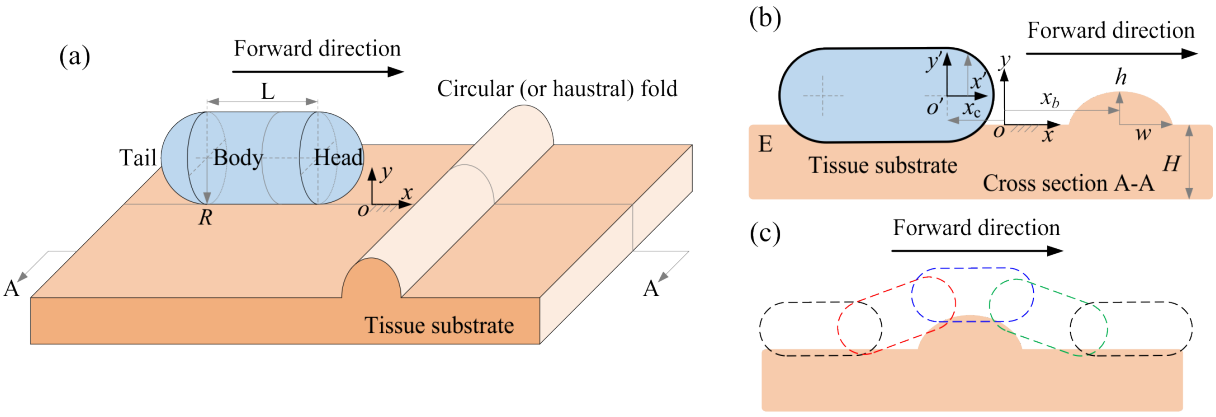

Figure 1: (Colour online) (a) 3D schematic diagram of a vibro-impact capsule robot moving on a piece of lower GI intestine in the presence of a circular (or haustral) fold. (b) Cross section A-A shows the inertial frame xoy and body frame $x'o'y'$, and the fold height, width, location, h, w and x_b, and tissue thickness and Young's modulus, H and E. (c) Schematic illustration of capsule gestures while it crosses over the fold, which has a pitch angle while it interacts with the fold.

The capsule includes a head, tail, and cylindrical body, whose cross sections can be further classified into five cases displayed in Figs. 2(b)-(f). More specifically, the vertical cross sections of the tail and head, as seen in Figs. 2(b) and (f), are circular. The cross section of the body displayed in Fig. 2(d) is perpendicular to the central axis of the capsule, which has a constant radius of R. By contrast, the vertical cross sections shown in Figs. 2(c) and (e) are more complex, which involve part of the spheric tail/head and part of the cylindrical body. Next, the resisting force and torque exerted on each part of the capsule will be calculated separately before summation for the overall resisting force and torque applied to the whole capsule.

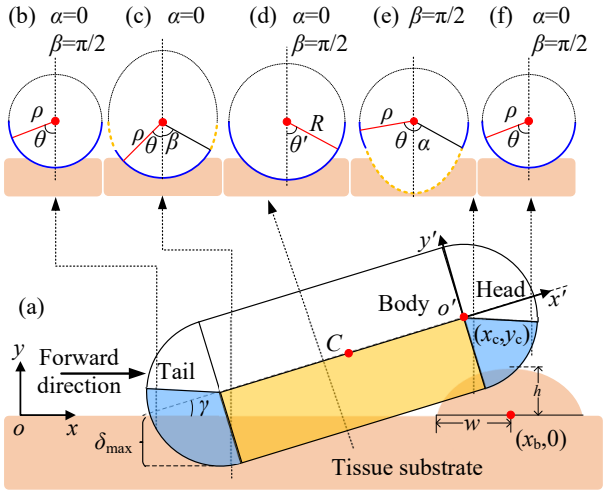

Figure 2: (Colour online) (a) A positive pitch angle and penetration depth ($\gamma > 0$ and $\delta_\mathrm{max} > 0$) when the capsule head contacts the fold. Only the coloured bottom are considered (blue for head and tail, and yellow for body) as the interactive area for the resisting force. The cross sections of different areas are displayed in Panels (b-f), where α and β are the lower and upper bounds of the contact angle (blue circle), θ and θ'.

2.2. Force on capsule head and tail

For the head ($x_\mathrm{c} < x \leq x_\mathrm{c} + R$) or the tail ($x_\mathrm{c} - L\cos(\gamma) - R < x \leq x_\mathrm{c} - L\cos(\gamma)$) of the capsule shown in Figs. 2(b-f), γ is the pitch angle of the capsule, whose vertical cross section is either part of or

a complete circle with a radius of

$$\rho(x) = \begin{cases} \sqrt{R^2 - (x - x_c)^2}, & \text{Head}, \\ \sqrt{R^2 - (x - x_c + L\cos(\gamma))^2}, & \text{Tail}. \end{cases} \tag{2}$$

Given Eq. (2), the bottom shape of capsule's head and tail can be described by the follow function

$$p(x, \theta) = \begin{cases} R + L\sin(\gamma) - \delta_{\max} - \rho(x)\cos(\theta), & \text{Head}, \\ R - \delta_{\max} - \rho(x)\cos(\theta), & \text{Tail}. \end{cases} \tag{3}$$

Wherever the tissue conforms to the capsule profile, the intestine deforms from its own shape function to the capsule's shape function, yielding the deformation

$$\delta(x, \theta) = \max\left(0, f(x) - p(x, \theta)\right). \tag{4}$$

Dividing the deformation by the original thickness of the substrate yields the tissue strain

$$\epsilon(x, \theta) = \frac{\delta(x, \theta)}{H + f(x)}. \tag{5}$$

The strain is then multiplied by the Young's module of the tissue, E, for the stress

$$\sigma(x, \theta) = \epsilon(x, \theta)E. \tag{6}$$

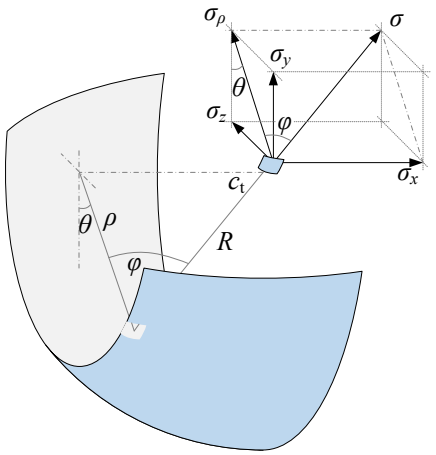

Figure 3: (Colour online) The stress, σ, exerts a normal pressure on the capsule, which can be decomposed into $x-$, $y-$ and $z-$directions.

It is seen in Fig. 3 that the stress exerts normal pressure on the capsule shell, which is mapped onto $x-$ and $y-$axes as

$$\begin{aligned} \sigma_x(x, \theta) &= \sigma(x, \theta)\sin(\varphi), \\ \sigma_y(x, \theta) &= \sigma(x, \theta)\cos(\varphi)\cos(\theta), \end{aligned} \tag{7}$$

where

$$\varphi(x) = \begin{cases} -\sin^{-1}\left(\frac{x - x_c}{R}\right), & \text{Head}, \\ -\sin^{-1}\left(\frac{x - x_c + L\cos(\gamma)}{R}\right), & \text{Tail}, \end{cases} \tag{8}$$

is the angle of anti-clockwise rotation from R to $\rho(x)$.

Integrating $\sigma_y(x,\theta)$ over the head and tail of the capsule shell gives the force exerted by the tissue on the head and tail which can be divided into two parts, and the vertical cross section of the first part is an incomplete circle. Integration of the contact angle has lower and upper limits, i.e., $\alpha \le \|\theta\| \le \beta$, which can be expressed as

$$\alpha = \begin{cases} 0, & -R < x - x_{\mathrm{c}} + L\cos(\gamma) < 0, \\ 0, & 0 < x - x_{\mathrm{c}} + L\cos(\gamma) < R\sin(\gamma), \\ \cos^{-1}\left(\frac{x-x_{\mathrm{c}}}{\rho(x)\tan(\gamma)}\right), & 0 < x - x_{\mathrm{c}} < R\sin(\gamma), \\ 0, & R\sin(\gamma) < x - x_{\mathrm{c}} < R, \end{cases} \tag{9}$$

$$\beta = \begin{cases} \frac{\pi}{2}, & -R < x - x_{\mathrm{c}} + L\cos(\gamma) < 0, \\ \cos^{-1}\left(\frac{x-x_{\mathrm{c}}+L\cos(\gamma)}{\rho(x)\tan(\gamma)}\right), & 0 < x - x_{\mathrm{c}} + L\cos(\gamma) < R\sin(\gamma), \\ \frac{\pi}{2}, & 0 < x - x_{\mathrm{c}} < R\sin(\gamma), \\ \frac{\pi}{2}, & R\sin(\gamma) < x - x_{\mathrm{c}} < R. \end{cases} \tag{10}$$

The contact force exerted on the capsule head is decomposed into vertical and horizontal directions, which can be obtained by the following integrations

$$\begin{aligned} F_y^{\mathrm{head}} =& 2\int_{x_{\mathrm{c}}}^{x_{\mathrm{c}}+R}\int_{\alpha}^{\beta}\sigma_y(x,\theta)\rho(x)\mathrm{d}\theta\frac{\mathrm{d}x}{\cos(\varphi(x))}, \\ F_x^{\mathrm{head}} =& 2\int_{x_{\mathrm{c}}}^{x_{\mathrm{c}}+R}\int_{\alpha}^{\beta}\sigma_x(x,\theta)\rho(x)\mathrm{d}\theta\frac{\mathrm{d}x}{\cos(\varphi(x))}. \end{aligned} \tag{11}$$

The corresponding torque about the centre of capsule is

$$\begin{aligned} M^{\mathrm{head}} =& 2\int_{x_{\mathrm{c}}}^{x_{\mathrm{c}}+R}\int_{\alpha}^{\beta}\sigma_y(x,\theta)(x-C_x)\rho(x)\mathrm{d}\theta\frac{\mathrm{d}x}{\cos(\varphi(x))} \\ &+2\int_{x_{\mathrm{c}}}^{x_{\mathrm{c}}+R}\int_{\alpha}^{\beta}\sigma_x(x,\theta)(C_y-p(x,\theta))\rho(x)\mathrm{d}\theta\frac{\mathrm{d}x}{\cos(\varphi(x))}, \end{aligned} \tag{12}$$

where

$$\begin{aligned} C_x &= x_c - \frac{L\cos(\gamma)}{2}, \\ C_y &= R - \delta_{\max} + \frac{L\sin(\gamma)}{2} \end{aligned} \tag{13}$$

are the coordinate of centre of mass of the capsule.

Similarly, the contact force applied to the capsule tail is

$$\begin{aligned} F_y^{\mathrm{tail}} &= 2\int_{x_{\mathrm{c}}-L\cos(\gamma)-R}^{x_{\mathrm{c}}-L\cos(\gamma)+R\sin(\gamma)}\int_{\alpha}^{\beta}\sigma_y(x,\theta)\rho(x)\mathrm{d}\theta\frac{\mathrm{d}x}{\cos(\varphi(x))}, \\ F_x^{\mathrm{tail}} &= 2\int_{x_{\mathrm{c}}-L\cos(\gamma)-R}^{x_{\mathrm{c}}-L\cos(\gamma)+R\sin(\gamma)}\int_{\alpha}^{\beta}\sigma_x(x,\theta)\rho(x)\mathrm{d}\theta\frac{\mathrm{d}x}{\cos(\varphi(x))}. \end{aligned} \tag{14}$$

The torque about the capsule centre from the tail is given by

$$\begin{aligned} M^{\text{tail}} = &2\int_{x_c-L\cos(\gamma)-R}^{x_c-L\cos(\gamma)+R\sin(\gamma)}\int_{\alpha}^{\beta}\sigma_y(x,\theta)(x-C_x)\rho(x)\mathrm{d}\theta\frac{\mathrm{d}x}{\cos(\varphi(x))} \\ &+2\int_{x_c-L\cos(\gamma)-R}^{x_c-L\cos(\gamma)+R\sin(\gamma)}\int_{\alpha}^{\beta}\sigma_x(x,\theta)(C_y-p(x,\theta))\rho(x)\mathrm{d}\theta\frac{\mathrm{d}x}{\cos(\varphi(x))}. \end{aligned} \tag{15}$$

2.3. Force on capsule body

For any given Point P on the capsule body, as shown in Fig. 4, one can find cross sections, which are perpendicular to x-axis (red) and x'-axis (grey), respectively. Letting the centres of the two cross sections as Points C and C', and the centre of the interaction line of the two cross sections as Point A, one obtains the relationship as follows

$$\begin{aligned} \overline{PC'}^2 &= \overline{AC'}^2 + \overline{AP}^2 \\ R^2 &= \overline{AC}^2\cos^2(\gamma) + \overline{AC}^2\tan^2(\theta) \end{aligned} \tag{16}$$

and

$$\begin{aligned} \overline{AP} &= \overline{AC'}\tan(\theta'), \\ \overline{AC}\tan(\theta) &= \overline{AC}\cos(\gamma)\tan(\theta'), \end{aligned} \tag{17}$$

where $\overline{AC}$ denotes the distance from Point A to Point C. Given Eq. (16), one obtains the distance between the centres of two cross sections, $d = \overline{CC'}$, as follows

$$d = \overline{AC}\sin(\gamma) = R\sin(\gamma)\sqrt{\frac{1}{\cos^2(\gamma)+\tan^2(\theta)}}. \tag{18}$$

Given Eq. (17), the coordinate of Point P can be transformed between the body and fixed frames by using

$$\begin{aligned} x &= (d+x')\cos(\gamma) + x_c, \\ \theta &= \tan^{-1}(\cos(\gamma)\tan(\theta')). \end{aligned} \tag{19}$$

Given the vertical movement and rotation of the capsule, the bottom of its body ($-L < x' < 0$) is given by the following shape function

$$\begin{aligned} p(x,\theta) =& R + (x - x_c + L\cos(\gamma))\tan(\gamma) \\ &- \sqrt{\frac{R^2}{\cos^2(\gamma)+\tan^2(\theta)}} - \delta_{\max}, \end{aligned} \tag{20}$$

which is then can be used with Eqs. (4), (5) and (6) to obtain the tissue stress on the capsule body, $\sigma(x,\theta)$. By using Eq. (19), the stress is then expressed in the body frame as follows

$$\begin{aligned} \sigma_{y'}(x',\theta') =& \sigma(x',\theta')\cos(\theta'), \\ \sigma_{x'}(x',\theta') =& 0. \end{aligned} \tag{21}$$

Integration of the stress in the body frame as follows yields the contact force

$$\begin{aligned} F_{y'}^{\text{body}} &= \int_{-L}^{0}\int_{-\frac{\pi}{2}}^{\frac{\pi}{2}}\sigma_{y'}(x',\theta')Rd\theta' dx', \\ F_{x'}^{\text{body}} &= 0. \end{aligned} \tag{22}$$

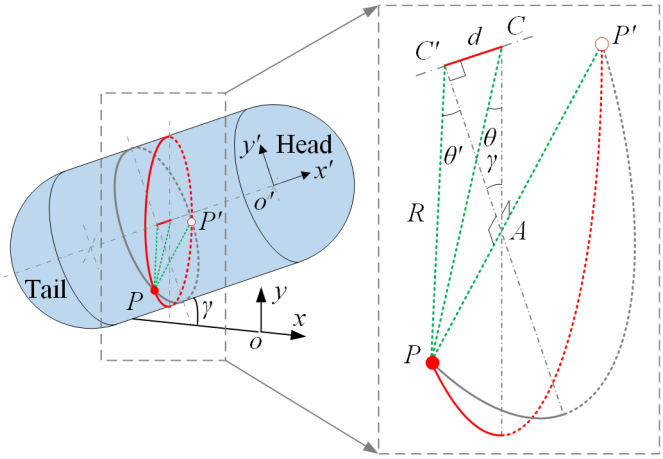

Figure 4: (Colour online) 3D illustration of the capsule, where one can find two cross sections passing Point P on the capsule shell. The red one is a vertical oval, with a contact angle θ, and its centre located at Point C. The grey section is perpendicular to the central axis of the capsule, which is a circle with a radius of R. The corresponding contact angle, θ', is defined in the body frame $x'o'y'$.

and torque

$$M^{\text{body}} = \int_{-L}^{0} \int_{-\frac{\pi}{2}}^{\frac{\pi}{2}} \sigma_{y'}(x', \theta') R \left(x' + \frac{L}{2} \right) d\theta' dx'. \tag{23}$$

After coordinate transformation, the stress in the natural coordinate system can be expressed as

$$\begin{bmatrix} F_x^{\text{body}} \\ F_y^{\text{body}} \end{bmatrix} = \begin{bmatrix} \cos(\gamma) & \sin(\gamma) \\ -\sin(\gamma) & \cos(\gamma) \end{bmatrix} \begin{bmatrix} 0 \\ F_{y'}^{\text{body}} \end{bmatrix}. \tag{24}$$

2.4. Resisting force

Next, summarising Eqs. (11), (14) and (24) yields the overall contact force exerted on the capsule due to tissue deformation as follows

$$\begin{aligned} F_x(x_c, \delta_{\max}, \gamma) &= F_x^{\text{head}} + F_x^{\text{tail}} + F_x^{\text{body}}, \\ F_y(x_c, \delta_{\max}, \gamma) &= F_y^{\text{head}} + F_y^{\text{tail}} + F_y^{\text{body}}. \end{aligned} \tag{25}$$

The overall corresponding torque is obtained by summarising Eqs. (12), (15) and (23) as follows

$$M(x_c, \delta_{\max}, \gamma) = M^{\text{head}} + M^{\text{tail}} + M^{\text{body}}. \tag{26}$$

For any given horizontal position, x_{c}, as the free body diagram displayed in Fig. 5(b), the capsule has external forces in $y-$direction and torques balanced, namely

$$\begin{cases} M(x_{\text{c}}, \delta_{\max}, \gamma) = 0, \\ F_y(x_c, \delta_{\max}, \gamma) = G. \end{cases} \tag{27}$$

Therefore, Eq. (27) implicitly determines the vertical displacement and rotation angle of the capsule, $\delta_{\max}(x_{\text{c}})$ and $\gamma(x_{\text{c}})$. As a result, the force in Eq. (25) can be regarded as a function of x_{c} for the resistance in $x-$direction, $F_x(x_{\text{c}})$, after γ and $\delta_{\max}$ are obtained by solving Eq. (27) numerically via Newton iteration.

2.5. Model of the vibro-impact capsule

A mathematical model of the vibro-impact capsule is displayed in Fig. 5(a), where the capsule shell has a mass of m_{c} [g], with an inner mass of m_{m} [g]. Therefore, the capsule gravity involves both of the inner

mass and the shell, i.e., $G = (m_\mathrm{m} + m_\mathrm{c})\, g$, where $g = 9810$ [mm s^{-2}] is the gravitational acceleration. The inner mass is connected to the capsule shell via a primary damped spring with a stiffness of k [N m^{-1}] and a damping coefficient of c [N s m^{-1}]. Besides, there are two extra springs in front of and behind the inner mass to constrain its motion. They have stiffness of k_1 [N m^{-1}] and k_2 [N m^{-1}], and gaps of g_1 [mm] and g_2 [mm], respectively.

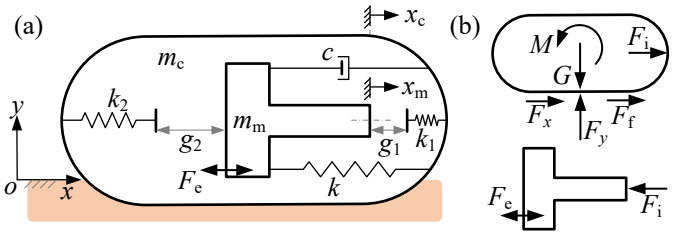

Figure 5: (Colour online) (a) Schematic of the vibro-impact capsule, which has an inner mass driven by an external periodic force, and interacts with the shell via a damped primary spring and two impact springs. (b) Free-body diagram of the capsule shell and the inner mass.

The inner mass is periodically driven by an external excitation as follows

$$F_\mathrm{e} = \begin{cases} P_d, & \mathrm{mod}(t, T) \in [0, DT], \\ 0, & \text{otherwise}, \end{cases} \tag{28}$$

where $\mathrm{mod}(t, T)$ indicates t modulo T, and P_d, T and $D \in (0\%,100\%)$ are the amplitude, period, and duty cycle ratio of the force, respectively. Via the primary and impact springs, the inner mass drives the capsule shell by the following piecewise linear interactive force

$$F_\mathrm{i} = \begin{cases} kx_r + cv_r + k_1 \left(x_r - g_1 \cos\gamma\right), & \text{if } x_r > g_1 \cos\gamma, \\ kx_r + cv_r + k_2 \left(x_r + g_2 \cos\gamma\right), & \text{if } x_r < -g_2 \cos\gamma, \\ kx_r + cv_r, & \text{otherwise}, \end{cases} \tag{29}$$

where $x_r = x_m - x_c$ and $v_r = \dot{x}_m - \dot{x}_c$ are the relative displacement and velocity between the inner mass and the capsule shell, and γ is the pitch angle.

Driven by F_i, the capsule shell may move either forward or backward, which is subjected to the reaction from the intestine including F_x and Coulomb friction, F_f [mN]. Depending on the moving speed and other forces, the frictional force is given by

$$F_\mathrm{f} = \begin{cases} -\mathrm{sign}(\dot{x}_c)\mu G, & \text{if } \dot{x}_c \neq 0, \\ -\mathrm{sign}(F_\mathrm{i} + F_x)\mu G, & \text{if } \dot{x}_c = 0 \text{ and } |F_\mathrm{i} + F_x| \geq \mu G, \\ -F_\mathrm{i} - F_x, & \text{if } \dot{x}_c = 0 \text{ and } |F_\mathrm{i} + F_x| < \mu G, \end{cases} \tag{30}$$

where $\mathrm{sign}(*)$ returns the sign of $*$, and μ is the frictional coefficient. Given all of the forces and free-body diagram in Fig. 5(b), the governing equation of the capsule robot can be written as

$$\begin{cases} m_m \ddot{x}_m = F_\mathrm{e} - F_\mathrm{i}, \\ m_c \ddot{x}_c = F_\mathrm{i} + F_x + F_\mathrm{f}. \end{cases} \tag{31}$$

3. Results and discussion

3.1. Model validation

In order to validate the new model given capsule rotation, its prediction of the resisting force has been compared with the model having translational movement only, finite element (FE) model, and

experimental testing studied in our previous works [43, 44, 48]. Figure 6 corresponds to the experimental setup, where the capsule successively crosses a small and a large folds. Compared with our previous model (Analytical-T) where the capsule translates only, the new model given general capsule motion (Analytical-G) has two more stages, Stages ③ and ⑤. As a result, the new model with the capsule climbing up and down the folds becomes compatible with the FE model and the experimental result.

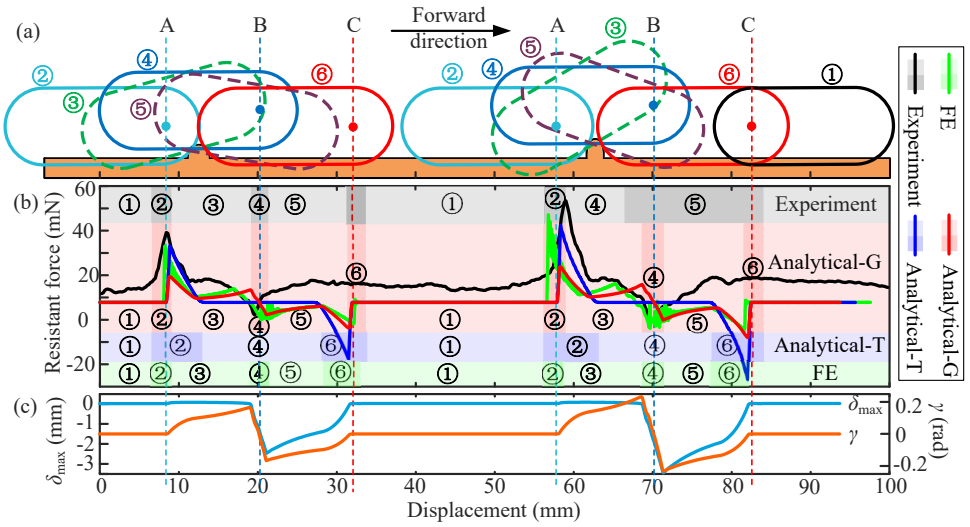

Figure 6: (Colour online) (a) Capsule gestures, (b) the horizontal resisting force, $-F_x$, exerted by the intestine and the folds on the capsule as a function of the capsule position, x_c, and (c) corresponding pitch angle and penetration depth, while the capsule passed over two different folds. The forces were respectively obtained from the Analytical-G model (red), the Analytical-T model (blue), FE analysis (green) and experiment (black). The process of fold crossing was divided into six stages, where only the Analytical-G and the FE models can capture all of the six stages. Corresponding parameters were chosen as $E = 100$ [kPa], $G = 33.96$ [mN], $\mu = 0.2293$, $R = 5.50$ [mm], $L = 15$ [mm], $H = 0.69$ [mm], $x_{b1} = 12.66$ [mm], $h_1 = 1.67$ [mm], $w_1 = 1.665$ [mm], $x_{b2} = 62.66$ [mm], $h_2 = 2.34$ [mm], $w_2 = 1.545$ [mm], which were identified from the experimental setup [49].

In general, the process of fold crossing can be divided into six stages. As shown in Fig. 6(a), in Stage ①, the capsule did not contact with any folds, and the resistance comes only from friction. Then the capsule moved forward to enter Stage ② once its head touched the fold, where the resisting force increased sharply towards its maximum. Then the capsule head pitched up in Stage ③, with a rapid drop before a slowly increase in resisting force. After the capsule's tail left the ground for a negative $\delta_{\max}$, the fold crossing entered Stage ④. The capsule stayed on the top of the fold, without its head or tail engaged with the tissue, where the resisting force underwent another drop as the capsule rotated to sink its head for a negative pitch angle. Then the capsule entered Stage ⑤ once its head touched the ground. The resisting force increased slightly before it decreased rapidly towards the minimum. This began Stage ⑥ where the capsule tail contacted the fold to push it forward. Then the capsule left the fold to re-enter Stage ①.

To illustrate the capsule's rotational and vertical motions during fold crossing process, the change of γ and $\delta_{\max}$ in the Analytical-G model are shown in Fig. 6(c). At State A, the capsule just touched the fold to climb up, where γ began to increase and the tail of the capsule became slightly embedded in the intestine, while the force on the capsule increased rapidly in Fig. 6(b). State B is the turning point, $\gamma = 0$, where the capsule starts to climb down the fold. The point is in the middle of Stage ④ where the capsule is on the top of the fold with only its body contacting with the tissue, and both of γ and $\delta_{\max}$ underwent sudden drops. State C is the opposite of State A, where the crossing process just ended, and the capsule regained its horizontal posture.

As illustrated in Fig. 6(b), both the new Analytical-G and FE models have all the six stages. Stage ⑥ was absent in the experiment, which could be induced by the fact that the experimental platform cannot measure a negative resisting force as it used a pulling string for force measurement. By contrast, the Analytical-T model did not have Stages ③ and ⑤ since the capsule cannot rotate in the model assumption. Compared with the Analytical-T (blue) model which had a stronger constrain on capsule motion, the Analytical-G (red) model yielded a much lower peak in resisting force. However, except the regions where

the FE model had drastic fluctuations in resisting force, the Analytical-G and FE models have consistent results, which is more obvious when the capsule climbed down the fold, i.e., Stages ⑤ and ⑥.

3.2. Influence of fold parameters

As mentioned above, all of the Analytical-T, Analytical-G, and FE models yielded similar results. We can therefore use them to evaluate the influence of fold parameters on the capsule's resisting force. If not otherwise specified, the following analysis used the default parameters listed in Table 1.

Table 1: Default parameters of the new model for simulations [50, 51].

Parameter	Symbol	Unit	Value
Capsule radius	R	mm	5.50
Capsule length	L	mm	15
Damping coefficient of the inner mass	c	Ns/m	0.0156
Right gap	g_1	mm	1.6
Left gap	g_2	mm	0
Stiffness of the primary spring	k	N/m	62
Stiffness of the second spring	k_1	N/m	27900
Stiffness of the tertiary spring	k_2	N/m	53500
Mass of the inner mass	m_{m}	g	1.8
Mass of the capsule	m_{c}	g	1.67
Young's Modulus of the intestine	E	kPa	100
Frictional coefficient	μ	-	0.2105
Thickness of the intestine	H	mm	0.69
Fold location	x_{b}	mm	12.66
Fold height	h	mm	1.67
Fold width	w	mm	1.665

The effect of height, width, Young's modulus and intestinal thickness on the resisting force is shown in Fig. 7. As seen, the Analytical-T model which does not rotate cannot capture the small extrema of resisting force arising in Stage ④. Figures 7(a)-(c) show a growth in the resisting force with respect to the increase of fold height. On the contrary, the resisting force in Figs. 7(d)-(f) decreases with respect to the increase of fold width. It is shown in Figs. 7(g)-(l) that decreasing thickness or increasing the Young's modulus of the intestine increases the resisting force mildly. No matter how the parameters change, the Analytical-G model always yielded consistent results compared with the FE model.

3.3. Critical driven force and bifurcation analysis

Next, Eq. (31) was numerically solved to study the capsule dynamics during its interaction with the fold. More specifically, Rung-Kutta method was adopted to simulate for 300 excitation periods, with the preceding 280 periods skipped to cut off the transient response and to record the steady response only. With all the other parameters fixed, the driven force, P_d, which was used as a bifurcation parameter, was gradually increased for forward simulation until the capsule successfully crossed the fold. Namely, each round of simulation used the final state of the model obtained from last round as initial condition.

To discuss the obstructive effect of the fold on the capsule locomotion, the steady-state dynamics of the capsule and its corresponding critical driven force before fold crossing were recorded and plotted as functions of other fold parameters. To illustrate, Fig. 8(a) shows an almost linear monotonic increase of the critical driven force with respect to the increase of fold height. For a small height, $h \leq 1.39$ [mm], the fold was crossed by a period-1 capsule motion (blue boundary). It was then changed to the non-periodic irregular dynamics for a higher fold (red), except a small region for 1.7 [mm] $\leq h \leq$ 1.8 [mm] (green), where the fold was crossed by a period-2 motion.

Then bifurcation diagrams for $h = 1.3$ [mm] and 3.3 [mm] are respectively displayed in Figs. 9 and 10, to illustrate the details of capsule dynamics before fold crossing. Corresponding time series of the capsule shell and inner mass, x_{c} and x_{m}, and phase portraits of the relative displacement and velocity, (x_{r} and v_{r}), are plotted for typical capsule dynamics. In addition, P-l-m-n was used to indicate a period-l motion of the capsule with m front and n back impacts on the constraints.

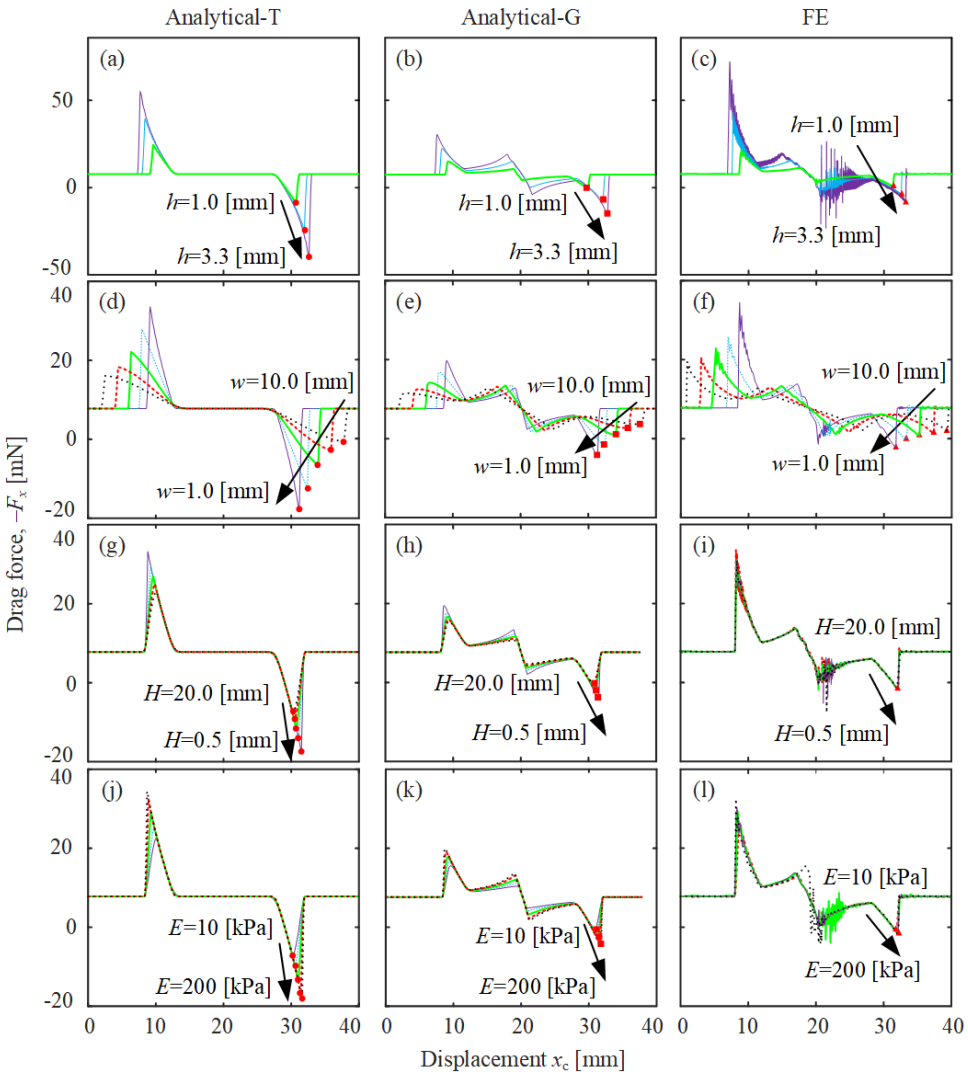

Figure 7: (Colour online) Resisting forces as functions of the capsule's position for various fold heights, widths, intestinal thickness and Young's moduli, where the left, middle and right columns were obtained by the Analytical-T, Analytical-G and FE models, respectively. The minima were marked by red squares, circles and triangles, respectively. (a)-(c) The fold height increases from 1.0 [mm] to 3,3 [mm]. (d)-(f) The fold width decreases from 10.0 [mm] to 1.0 [mm]. (g)-(i) The intestinal thickness changes from 20.0 [mm] to 0.5 [mm]. (j)-(l) Young's modulus of the intestine fchanges from 10 [kPa] to 200 [kPa].

The lower fold for $h = 1.3$ [mm] displays a simple bifurcation pattern in Fig. 9. The capsule performed a P-1-2-0 motion for a small driven force, $P_d \leq 18.2$ [mN], which thereafter bifurcated into a P-3-5-0 motion. Then this period-3 motion became non-periodic irregular for $P_d \geq 19.6$ [mN]. The capsule motion then changed back to the P-1-2-0 motion for $P_d \geq 21.2$ [mN] before the fold crossing for $P_d > 21.4$ [mN].

Compared with the lower fold, the higher fold for $h = 3.3$ [mm] required a larger critical driven force and induced more complex dynamics before fold crossing. As displayed in Fig. 10(a), the capsule displayed a P-1-2-0 motion for a small driven force, $P_d \leq 10$ [mN]. It then underwent period doubling bifurcations to be P-2-4-0 for $P_d \leq 12.6$ [mN] and P-4-7-0 for $P_d \leq 16.4$ [mN]. Next, a reverse period doubling bifurcation for $P_d = 16.6$ [mN] and another period doubling bifurcation for $P_d = 16.6$ [mN] switched the capsule dynamics between P-2-4-0 and P-4-7-0. For $P_d \geq 22.2$ [mN], the majority of the capsule motions are non-periodic irregular, except some windows for P-6-6-0 ($P_d = 23.6$ [mN]), P-2-1-0 (24.6 [mN] $\leq P_d \leq$ 25.2 [mN]), P-2-2-0 (27.4 [mN] $\leq P_d \leq$ 28 [mN] and 29.6 [mN] $\leq P_d \leq$ 30.4 [mN]),

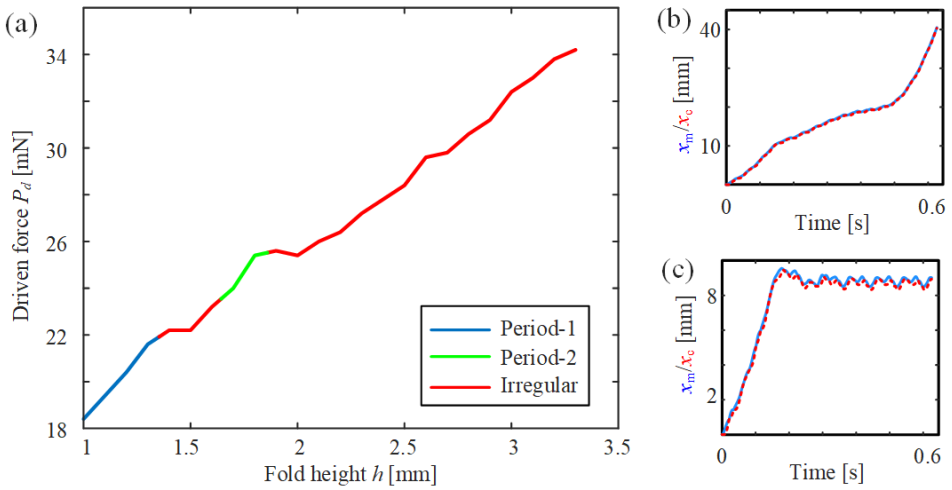

Figure 8: (Colour online) (a) Critical boundary of the driven force which is sufficient for the capsule to cross over the fold. Typical time series of the capsule shell (red) and inner mass (blue) for the parameters under and over the boundary (unsuccessful and successful crossing) are displayed in Panels (b) and (c), respectively. The critical boundary is marked with different colours for the steady-state capsule dynamics before fold crossing, which are blue, green and red for the period-1, period-2 and irregular motions, respectively.

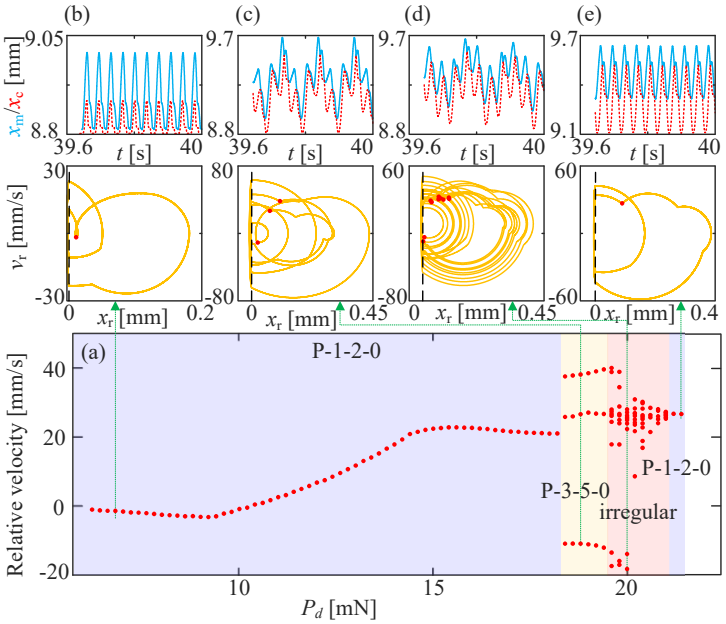

Figure 9: (Colour online) (a) Bifurcation diagram of the capsule dynamics for $h = 1.3$ [mm], where the Poincaré sections of the relative velocity are plotted as functions of the driven force. Time series and phase portraits for $P_d = 6.8$ [mN], 18.8 [mN], 20 [mN], and 21.4 [mN] are displayed in Panels (b-e) to illustrate the P-1-2-0, P-3-5-0, irregular, and P-1-2-0 motions in each region. Here, P-l-m-n denotes the period-l motion of the capsule with m front and n back impacts on the constraints.

and P-4-3-0 ($P_d = 28.2$ [mN] and 29.2 [mN] $\leq P_d \leq 29.4$ [mN]). Therefore, the fold was finally crossed by irregular motions for $P_d \geq 34.4$ [mN].

Then the influence of fold width, w, on the critical boundary was displayed in Fig. 11(a). It is seen that the critical driven force for fold crossing gradually decreased with respect to the increase of fold width. A thin fold, $w \leq 1.5$ [mm], which yielded large resisting force, was finally crossed via the period-2 motion. A typical bifurcation diagram for $w = 1.5$ [mm] is correspondingly displayed in Fig. 11(b). It is

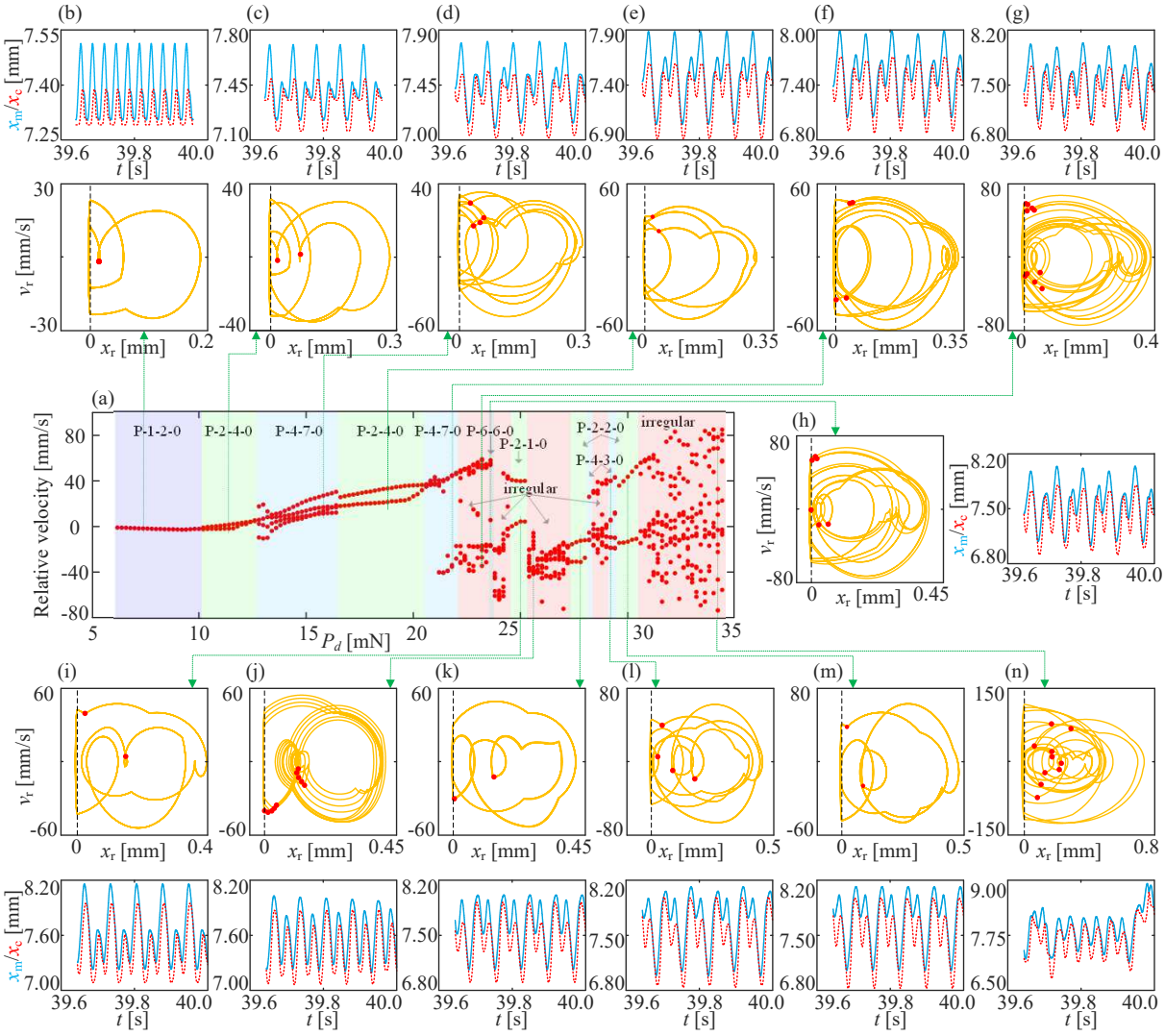

Figure 10: (Colour online) (a) Bifurcation diagram of the capsule dynamics for $h = 3.3$ [mm], where the Poincaré section of the relative velocity is plotted as a function of the driven force. Time series and phase portraits for $P_d = 7.4$ [mN], 11.4 [mN], 15.8 [mN], 18.6 [mN], 21.8 [mN], 23.2 [mN], 23.6 [mN], 25 [mN], 25.6 [mN], 27.8 [mN], 29.2 [mN], 30 [mN], and 34.2 [mN] are displayed in Panels (b-n) respectively to illustrate the P-1-2-0, P-2-4-0, P-4-7-0, P-2-4-0, irregular, P-2-1-0, irregular, P-2-2-0, P-4-3-0, P-2-2-0, and irregular motions in each region.

seen that the capsule dynamics for the small driven force, $P_d \leq 15$ [mN] was P-1-2-0, which underwent period doubling for the P-2-4-0 motion for $P_d \leq 17.2$ [mN]. Then a small window of irregular motion ($P_d = 17.4$ [mN]) changed the capsule dynamics into P-2-3-0 before fold crossing, with one less back impact compared with the preceding state. The critical boundary was then changed to red for irregular motion in the vicinity of $w = 2$ [mm] , which yielded the bifurcation pattern in Fig. 11(c) very similar to that in Fig. 11(b), except that the capsule motion finally became irregular before fold crossing. For the wider folds, $w \geq 2.5$ [mm], the critical boundary is always blue, indicating the period-1 motion for fold crossing. However, the bifurcation pattern could be different as well. For example, Fig. 11(e) for $w = 5$ [mm] displays the P-1-2-0 motion without any bifurcation. By contrast, Fig. 11(d) for $w = 4$ [mm] has small windows for P-3-6-0 (16.6 [mm] $\leq P_d \leq$ 17.4 [mm]) and irregular (17.6 [mN] $\leq P_d \leq$ 18.4 [mm]) responses.

As seen in Figs. 11 and 12, increasing the intestine thickness has very similar effect on the critical boundary and bifurcation pattern compared with increasing the fold width. Namely, the critical driven force decreased with respect to the increase of H, which also changed from a period-2 motion (green) to

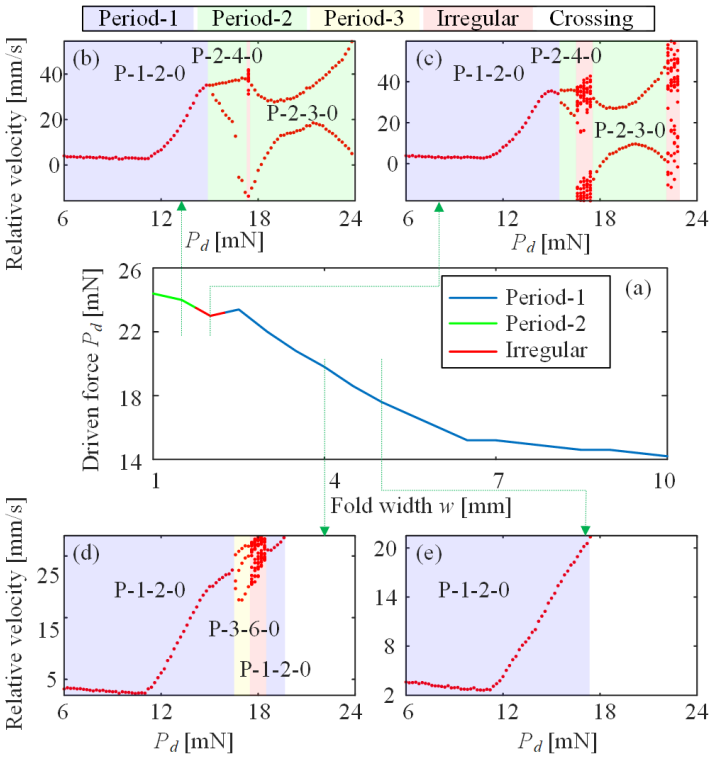

Figure 11: (Colour online) (a) Critical boundary of the driven force for fold crossing is plotted as a function of the fold width. Corresponding bifurcation diagrams are displayed for (b) $w = 1.5$ [mm], (c) $w = 2$ [mm], (d) $w = 4$ [mm], and (e) $w = 5$ [mm].

irregular (red) and period-1 motion (blue). Moreover, the bifurcation patterns in Figs. 12(b), (d) and (e) are similar to those in Figs. 11(b), (d) and (e). The most significant difference is the bifurcation in Fig. 12(c), which became irregular directly from P-1-2-0 for $P_d \geq 17.2$ [mN], without further bifurcation before the fold crossing for $P_d > 17.2$ [mN].

Influence of Young's modulus of the intestine on the critical driven force is displayed in Fig. 13. The boundary increased with respect to the enhancement of Young's modulus at the beginning, which a gradual decrease of the increasing rate. In addition, the boundary in this region, $E < 55$ [kPa], was always blue for period-1 motion. After the increasing of driven fore was leveled off for $E \geq 60$ [kPa], the boundary changed to red for irregular motions. In general, the bifurcation in Figs. 13(b), (d) and (e) has similar patterns found in Figs. 11 and 12. However, the bifurcation in Fig. 13(c) induced a P-5-8-0 motion for 18 [mN] $\leq P_d \leq$ 20.4 [mN] before the bifurcation into irregular and thereafter the P-1-2-0 motion for fold crossing.

To sum up, the obstructive effect of the fold on capsule locomotion is more significant for a larger resisting force, which corresponds with large fold height, small fold width, small thickness of the intestine and large Young's modulus. In case of small resisting force, the capsule dynamics keeps P-1-2-0, without any bifurcation before fold crossing. For large resisting force, The capsule requires higher driven force to cross fold. In addition, the increase of driven force induces various complex bifurcation to the capsule dynamics, so the fold is crossed mainly by irregular and period-2 responses in case of a large resisting force.

4. Conclusions

This paper proposed a new model for a vibro-impact capsule robot self-propelling in the lower GI tract. The model was used for evaluating the resisting force of the intestine on the robot. Then it was

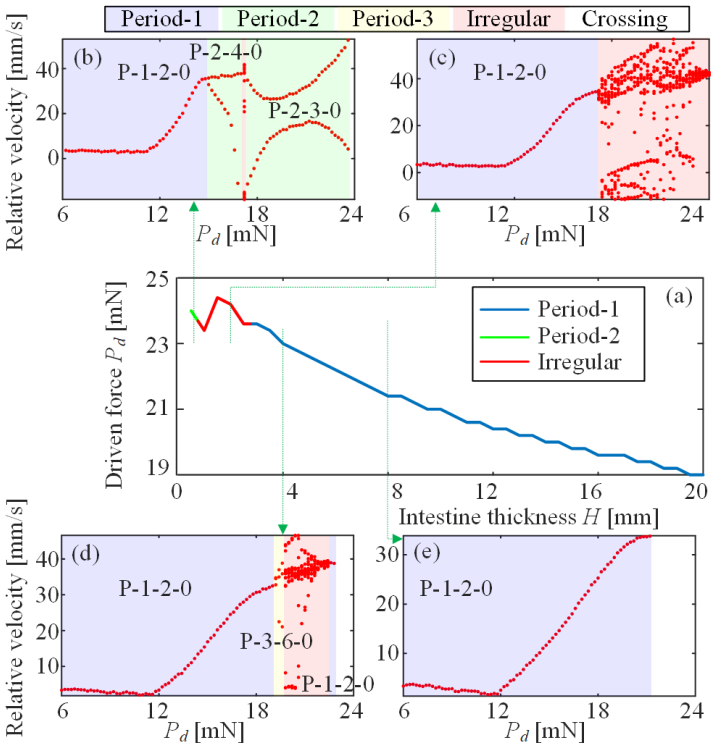

Figure 12: (Colour online) (a) Critical boundary of the driven force for fold crossing is plotted as a function of the intestine thickness. Corresponding bifurcation diagrams are displayed for (b) $H = 0.6$ [mm], (c) $H = 2$ [mm], (d) $H = 4$ [mm], and (e) $H = 8$ [mm].

further used for the study of the capsule dynamics under different intestinal properties, such as fold height and width, intestine thickness, and Young's modulus of the intestine.

Compared with our previous studies, the new model of resisting force considered capsule rotation, which addressed the issue of absence of pitch angle during the fold crossing process. As a result, the new model included all the six stages of fold crossing and yielded a more consistent result compared with the FE model.

Then the influence of fold parameters on the resisting force was studied, yielding a larger force in the case of a higher and thinner fold on a thinner and stiffer intestine. Moreover, the influence of fold geometry is more significant compared with the thickness and Young's modulus of the intestine.

Finally, the capsule dynamics interacting with the fold was investigated by numerical simulation and bifurcation analysis. It was found that the fold with a large resisting force is much harder to be crossed i.e., it requires a larger driven force to overcome the obstruction. For a small resisting force, the capsule always performed the period-1 motion with two back impacts, without any bifurcation into complex dynamics before fold crossing. For a large resisting force, on the contrary, the P-1-2-0 motion can bifurcate into various complex periodic or non-periodic responses. Thus, period-2 and irregular motions were observed frequently before fold crossing in case of large resisting forces.

Acknowledgments

Professor Yao Yan was supported by the National Natural Science Foundation of China (Grants No. 12072068, 11932015, 52175046, and 11872147) and the Sichuan Science and Technology Program (Grant No. 2022JDRC0018).

Compliance with ethical standards.

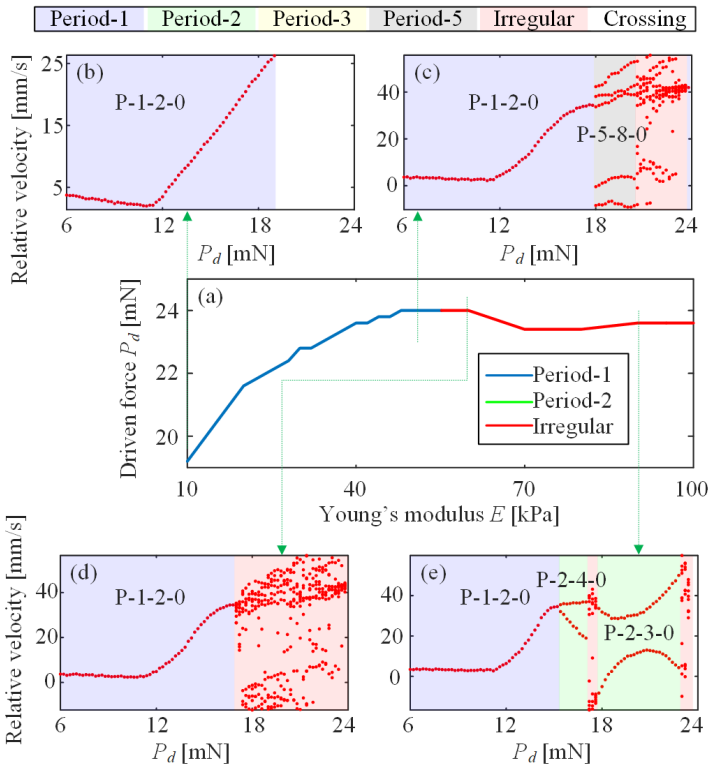

Figure 13: (Colour online) (a) Critical boundary of the driven force for fold crossing is plotted as a function of the Young's modulus. Corresponding bifurcation diagrams are displayed for (b) $E = 10$ [kPa], (c) $E = 50$ [kPa], (d) $E = 60$ [kPa], and (e) $E = 90$ [kPa].

Conflict of interest. The authors declare that they have no conflict of interest concerning the publication of this manuscript.

Data accessibility. The numerical and experimental data sets generated and analysed during the current study are available from the corresponding author on reasonable request.

References

[1] S. Bouchard, M. Ibrahim, and A. Van Gossum, "Video capsule endoscopy: perspectives of a revolutionary technique," *World Journal of Gastroenterology*, vol. 20, no. 46, pp. 17330–17344, 2014.

[2] E. C. Marginean, "The ever-changing landscape of drug-induced injury of the lower gastrointestinal tract," *Archives of Pathology & Laboratory Medicine*, vol. 140, no. 8, pp. 748–758, 2016.

[3] K. Liu and A. Kaffes, "The diagnosis and investigation of obscure gastrointestinal bleeding," *Alimentary Pharmacology & Therapeutics*, vol. 34, no. 4, pp. 416–423, 2011.

[4] C. Langner, D. Aust, A. Ensari, V. Villanacci, G. Becheanu, S. Miehlke, K. Geboes, A. Münch, W. G. of Digestive Diseases of the European Society of Pathology (ESP), and the European Microscopic Colitis Group (EMCG), "Histology of microscopic colitis—review with a practical approach for pathologists," *Histopathology*, vol. 66, no. 5, pp. 613–626, 2015.

[5] R. Patel and W. Hyer, "Practical management of polyposis syndromes," *Frontline Gastroenterology*, vol. 10, no. 4, pp. 379–387, 2019.

[6] A. Koulaouzidis and G. Baatrup, "Current status of colon capsule endoscopy in clinical practice," *Nature Reviews Gastroenterology & Hepatology*, pp. 1–2, 2023.

[7] H. Wahab, I. Mehmood, H. Ugail, A. K. Sangaiah, and K. Muhammad, "Machine learning based small bowel video capsule endoscopy analysis: Challenges and opportunities," *Future Generation Computer Systems*, 2023.

[8] H. M. Kim, S. Yang, J. Kim, S. Park, J. H. Cho, J. Y. Park, T. S. Kim, E.-S. Yoon, S. Y. Song, and S. Bang, "Active locomotion of a paddling-based capsule endoscope in an in vitro and in vivo experiment (with videos)," *Gastrointestinal Endoscopy*, vol. 72, no. 2, pp. 381–387, 2010.

[9] Z.-J. Sun, B. Ye, Y. Qiu, X.-G. Cheng, H.-H. Zhang, and S. Liu, "Preliminary study of a legged capsule robot actuated wirelessly by magnetic torque," *IEEE Transactions on Magnetics*, vol. 50, no. 8, pp. 1–6, 2014.

[10] J. Gao and G. Yan, "Locomotion analysis of an inchworm-like capsule robot in the intestinal tract," *IEEE Transactions on Biomedical Engineering*, vol. 63, no. 2, pp. 300–310, 2015.

[11] R. Carta, G. Tortora, J. Thoné, B. Lenaerts, P. Valdastri, A. Menciassi, P. Dario, and R. Puers, "Wireless powering for a self-propelled and steerable endoscopic capsule for stomach inspection," *Biosensors and Bioelectronics*, vol. 25, no. 4, pp. 845–851, 2009.

[12] Y. Liu, M. Wiercigroch, E. Pavlovskaia, and H. Yu, "Modelling of a vibro-impact capsule system," *International Journal of Mechanical Sciences*, vol. 66, pp. 2–11, 2013.

[13] M. Sfakiotakis, N. Pateromichelakis, and D. P. Tsakiris, "Vibration-induced frictional reduction in miniature intracorporeal robots," *IEEE Transactions on Robotics*, vol. 30, no. 5, pp. 1210–1221, 2014.

[14] H. Zhou, G. Alici, T. D. Than, and W. Li, "Modeling and experimental characterization of propulsion of a spiral-type microrobot for medical use in gastrointestinal tract," *IEEE Transactions on Biomedical Engineering*, vol. 60, no. 6, pp. 1751–1759, 2012.

[15] F. L. Chernous'ko, "The optimum rectilinear motion of a two-mass system," *Journal of Applied Mathematics and Mechanics*, vol. 66, no. 1, pp. 1–7, 2002.

[16] M. Liao, Y. Liu, J. Páez Chávez, A. S. Chong, and M. Wiercigroch, "Dynamics of vibro-impact drilling with linear and nonlinear rock models," *International Journal of Mechanical Sciences*, vol. 146, pp. 200–210, 2018.

[17] B. Guo, E. Ley, J. Tian, J. Zhang, Y. Liu, and S. Prasad, "Experimental and numerical studies of intestinal frictions for propulsive force optimisation of a vibro-impact capsule system," *Nonlinear Dynamics*, vol. 101, no. 1, pp. 65–83, 2020.

[18] Y. Yan, Y. Liu, H. Jiang, Z. Peng, A. Crawford, J. Williamson, J. Thomson, G. Kerins, A. Yusupov, and S. Islam, "Optimization and experimental verification of the vibro-impact capsule system in fluid pipeline," *Proceedings of the Institution of Mechanical Engineers, Part C: Journal of Mechanical Engineering Science*, vol. 233, no. 3, pp. 880–894, 2019.

[19] Y. Liu, E. Pavlovskaia, D. Hendry, and M. Wiercigroch, "Vibro-impact responses of capsule system with various friction models," *International Journal of Mechanical Sciences*, vol. 72, pp. 39–54, 2013.

[20] K. O. Afebu, J. Tian, Y. Liu, E. Papatheou, and S. Prasad, "Ai-assisted dynamic tissue evaluation for early bowel cancer diagnosis using a vibrational capsule," *IEEE Robotics and Automation Letters*, vol. 8, no. 4, pp. 2341–2348, 2023.

[21] J. Zhang, Y. Liu, J. Tian, D. Zhu, and S. Prasad, "Design and experimental investigation of a vibro-impact capsule robot for colonoscopy," *IEEE Robotics and Automation Letters*, vol. 8, no. 3, pp. 1842–1849, 2023.

[22] J. Zhang, J. Tian, D. Zhu, Y. Liu, and S. Prasad, "Design and experimental investigation of a vibro-impact self-propelled capsule robot with orientation control," in *2022 International Conference on Robotics and Automation (ICRA)*, pp. 11381–11387, IEEE, 2022.

[23] T. Rahim, M. A. Usman, and S. Y. Shin, "A survey on contemporary computer-aided tumor, polyp, and ulcer detection methods in wireless capsule endoscopy imaging," *Computerized Medical Imaging and Graphics*, vol. 85, p. 101767, 2020.

[24] Medtronic, "PILLCAM™ SB 3 system, Medtronic: capsule endoscopy products." Accessed: 16 September 2020.

[25] Y. Liu, J. Páez Chávez, J. Zhang, J. Tian, B. Guo, and S. Prasad, "The vibro-impact capsule system in millimetre scale: Numerical optimisation and experimental verification," *Meccanica*, vol. 55, no. 10, pp. 1885–1902, 2020.

[26] V.-D. Nguyen, T.-H. Duong, N.-H. Chu, and Q.-H. Ngo, "The effect of inertial mass and excitation frequency on a duffing vibro-impact drifting system," *International Journal of Mechanical Sciences*, vol. 124, pp. 9–21, 2017.

[27] T.-H. Duong, V.-D. Nguyen, H.-C. Nguyen, N.-P. Vu, N.-K. Ngo, and V.-T. Nguyen, "A new design for bidirectional autogenous mobile systems with two-side drifting impact oscillator," *International Journal of Mechanical Sciences*, vol. 140, pp. 325–338, 2018.

[28] Y. Yan, Y. Liu, L. Manfredi, and S. Prasad, "Modelling of a vibro-impact self-propelled capsule in the small intestine," *Nonlinear Dynamics*, vol. 96, no. 1, pp. 123–144, 2019.

[29] B. Guo, Y. Liu, R. Birler, and S. Prasad, "Self-propelled capsule endoscopy for small-bowel examination: proof-of-concept and model verification," *International Journal of Mechanical Sciences*, vol. 174, p. 105506, 2020.

[30] Y. Liu, J. Páez Chávez, B. Guo, and R. Birler, "Bifurcation analysis of a vibro-impact experimental rig with two-sided constraint," *Meccanica*, pp. 1–17, 2020.

[31] J. E. Hall, *Guyton and Hall Textbook of Medical Physiology*. Jordan: Elsevier, 1st ed., 2016.

[32] W. Hohenberger and M. Parker, *Lower gastrointestinal tract surgery: Vol. 2, open procedures*. Springer Nature, 2021.

[33] A. M. DiGregorio and H. Alvey, "Gastrointestinal bleeding," in *StatPearls [internet]*, StatPearls Publishing, 2021.

[34] S. Standring, "The anatomy of the large intestine," *Lower Gastrointestinal Tract Surgery: Vol. 1, Laparoscopic procedures*, pp. 27–89, 2019.

[35] M. Smith and D. Morton, *The Digestive System, Basic Science and Clinical Conditions*. Toronto: Elsevier, 2nd ed., 2010.

[36] L. Barducci, J. C. Norton, S. Sarker, S. Mohammed, R. Jones, P. Valdastri, and B. S. Terry, "Fundamentals of the gut for capsule engineers," *Progress in Biomedical Engineering*, vol. 2, no. 4, p. 042002, 2020.

[37] H. Ellis, "Anatomy of the small intestine (jejunum and ileum)," *Surgery (Oxford)*, vol. 29, pp. 355–357, 2011.

[38] M. P. Federle, M. L. Rosado-de Christenson, S. P. Raman, B. W. Carter, P. J. Woodward, and A. M. Shaaban, *Imaging Anatomy: Chest, Abdomen, Pelvis E-Book*. Philadelphia: Elsevier, 2nd ed., 2017.

[39] C. G. Cronin, E. Delappe, D. G. Lohan, C. Roche, and J. M. Murphy, "Normal small bowel wall characteristics on MR enterography," *European Journal of Radiology*, vol. 75, no. 2, pp. 207–211, 2010.

[40] J. D. Huizinga, M. Pervez, S. Nirmalathasan, and J.-H. Chen, "Characterization of haustral activity in the human colon," *American Journal of Physiology-Gastrointestinal and Liver Physiology*, vol. 320, no. 6, pp. G1067–G1080, 2021.

[41] A. C. Thompson, R. H. Jones, P. D. Poullos, S. Banerjee, and L. K. Shin, "Taller haustral folds in the proximal colon: A potential factor contributing to interval colorectal cancer," *Journal of Colon and Rectal Cancer*, vol. 1, no. 1, pp. 45–54, 2016.

[42] J. Tian, K. O. Afebu, A. Bickerdike, Y. Liu, S. Prasad, and B. J. Nelson, "Fundamentals of bowel cancer for biomedical engineers," *Annals of Biomedical Engineering*, vol. 51, no. 4, pp. 679–701, 2023.

[43] Y. Yan, B. Guo, J. Tian, J. Zhang, B. Zhang, E. Ley, Y. Liu, and S. Prasad, "Evaluating the resistant force of an endoscopic capsule self-propelling in the small intestine," *Archive of Applied Mechanics*, vol. 92, no. 12, pp. 3861–3875, 2022.

[44] Y. Yan, B. Zhang, J. Páez Chávez, and Y. Liu, "Optimising the locomotion of a vibro-impact capsule robot self-propelling in the small intestine," *Communications in Nonlinear Science and Numerical Simulation*, vol. 114, p. 106696, 2022.

[45] S. Yin, Y. Yan, J. Páez Chávez, and Y. Liu, "Bifurcation analysis of a vibro-impacting capsule robot in contact with a circular fold," *Physica D: Nonlinear Phenomena*, vol. 442, p. 133524, 2022.

[46] S. Yin, Y. Yan, J. Páez Chávez, and Y. Liu, "Dynamics of a self-propelled capsule robot in contact with different folds in the small intestine," *Communications in Nonlinear Science and Numerical Simulation*, vol. 126, p. 107445, 2023.

[47] L. J. Sliker, G. Ciuti, M. E. Rentschler, and A. Menciassi, "Frictional resistance model for tissue-capsule endoscope sliding contact in the gastrointestinal tract," *Tribology International*, vol. 102, pp. 472–484, 2016.

[48] Y. Yan, B. Zhang, Y. Liu, and S. Prasad, "Dynamics of a vibro-impact self-propelled capsule encountering a circular fold in the small intestine," *Meccanica*, vol. 58, no. 2, pp. 451–472, 2023.

[49] B. Guo, Y. Liu, and S. Prasad, "Modelling of capsule–intestine contact for a self-propelled capsule robot via experimental and numerical investigation," *Nonlinear Dynamics*, vol. 98, no. 4, pp. 3155–3167, 2019.

[50] B. Guo, E. Ley, J. Tian, J. Zhang, Y. Liu, and S. Prasad, "Experimental and numerical studies of intestinal frictions for propulsive force optimisation of a vibro-impact capsule system," *Nonlinear Dynamics*, vol. 101, no. 1, pp. 65–83, 2020.

[51] Y. Liu, J. Páez Chávez, J. Zhang, J. Tian, B. Guo, and S. Prasad, "The vibro-impact capsule system in millimetre scale: numerical optimisation and experimental verification," *Meccanica*, vol. 55, no. 10, pp. 1885–1902, 2020.